sensors

MDPI

Article

Experimental and Numerical Studies of the Temperature Field in a Dielectrophoretic Cell Separation Device Subject to Joule Heating

Yoshinori Seki and Shigeru Tada *

Department of Applied Physics, National Defense Academy, Hashirimizu 1-10-20, Yokosuka City 239-0802, Kanagawa, Japan; ed22004@nda.ac.jp
* Correspondence: stada@nda.ac.jp; Tel.: +81-46-841-3810

Abstract: Technologies for rapid and high-throughput separation of rare cells from large populations of other types of cells have recently attracted much attention in the field of bioengineering. Among the various cell separation technologies proposed in the past, dielectrophoresis has shown particular promise because of its preciseness of manipulation and noninvasiveness to cells. However, one drawback of dielectrophoresis devices is that their application of high voltage generates Joule heat that exposes the cells within the device to high temperatures. To further explore this problem, this study investigated the temperature field in a previously developed cell separation device in detail. The temperature rise at the bottom of the microfluidic channel in the device was measured using a micro-LIF method. Moreover, the thermofluidic behavior of the cell separation device was numerically investigated by adopting a heat generation model that takes the electric-field-dependent heat generation term into account in the energy equation. Under the operating conditions of the previously developed cell separation device, the experimentally obtained temperature rise in the device was approximately 20 °C, and the numerical simulation results generally agreed well. Next, parametric calculations were performed with changes in the flow rate of the cell sample solution and the solution conductivity, and a temperature increase of more than 40 °C was predicted. The results demonstrated that an increase in temperature within the cell separation device may have a significant impact on the physiological functions of the cells, depending on the operating conditions of the device.

Keywords: dielectrophoresis; microfluidics; Joule heat; numerical simulation; micro-LIF method

check for updates

Citation: Seki, Y.; Tada, S. Experimental and Numerical Studies of the Temperature Field in a Dielectrophoretic Cell Separation Device Subject to Joule Heating. *Sensors* **2024**, *24*, 7098. https://doi.org/10.3390/s24217098

Academic Editors: Shengyong Xu and Jingjing Xu

Received: 7 October 2024
Revised: 1 November 2024
Accepted: 2 November 2024
Published: 4 November 2024

Copyright: © 2024 by the authors. Licensee MDPI, Basel, Switzerland. This article is an open access article distributed under the terms and conditions of the Creative Commons Attribution (CC BY) license (https://creativecommons.org/licenses/by/4.0/).

1. Introduction

Recently, dielectrophoresis (DEP) has been attracting attention as a technique for separating rare cells from a large number of cells [1–3]. DEP is a phenomenon in which dielectric microparticles placed in a nonuniform electric field move under the force along the gradient of the electric field [4], and this principle can be used to manipulate cells noninvasively and with high precision. The application of the DEP principle utilizing an A.C. electric field makes it possible to selectively manipulate biological microparticles, such as cells, with high precision according to their inherent electrical properties. This capability contributes to the development of critical fundamental technologies in life sciences, such as cell separation, concentration, purification, and manipulation technologies. Therefore, there is a strong demand for the development of rapid and high-precision cell separation technologies that leverage the advantages of DEP [5–7].

Among the many forms of DEP-based microdevices, electrode-based dielectrophoresis (eDEP) devices are distinguished by the large electric field gradient generated within the microdevice by microelectrodes [8–11]. By applying an A.C. voltage to an eDEP device, a large electric field gradient is generated around the fine electrodes, and this electric field gradient generates a DEP force that acts on cells. Because the electric field gradient

determines the magnitude and direction of the DEP force acting on cells, it is necessary to generate within the device an electric field of adequate strength to manipulate target cells with high precision. However, cell separation devices based on dielectrophoresis have the drawback that the cells inside the device are exposed to a high-temperature environment due to Joule heating [12,13]. The degree of Joule heating mostly depends on the square of the electric field magnitude [14,15]. Thus, there is a risk that cells inside the device are exposed to a high-temperature environment due to the Joule heat generated by the application of high voltage [16,17].

It has been confirmed that high-temperature exposure may affect the physiological functionality of cells [18]. Moritz et al. conducted experiments using human and porcine epidermal cells and reported that irreversible cell damage occurs when the cells are exposed to a high-temperature environment above 44 °C for approximately 6 h [19]. Harmon et al. reported that apoptosis was significantly promoted by exposing murine mastocytoma cells to a high-temperature environment of around 44 °C [20]. Yamada et al. reported that cell division was halted when MKN-1 and SNG-M cells were exposed to a high-temperature environment of 42 °C [21]. Consequently, recent studies have focused on Joule heating and temperature fields within dielectrophoresis-based cell separation devices to evaluate their effects on cells [22–24]. In particular, the correlation between solution conductivity and the temperature increase has been extensively investigated. For example, Tay et al. measured the temperature field of planar electrodes using a NaCl solution with $\sigma_f = 1$ S/m and reported a temperature rise of up to 100 °C [22]. Sridharan et al. conducted an observation experiment on fluid circulation within a device using a phosphate-buffered solution with $\sigma_f = 4.7 \times 10^{-2}$ S/m and predicted a temperature change of about 30 °C in their numerical simulations [23]. Nakano et al. measured the temperature field within an insulated DEP (iDEP) device using a phosphate-buffered solution with $\sigma_f = 1.0 \times 10^{-1}$ S/m and found that the temperature rose about 70 °C [24]. Among other relevant studies that measured the temperature rise due to Joule heating in microdevices, Williams et al. measured the temperature using the laser-induced fluorescence (LIF) method with varying solution conductivity and applied voltage [25]. Pramod et al. measured the nonuniform temperature profiles in a silicon microchannel heat sink due to Joule heating and flow maldistribution using the micro-LIF method [26,27].

Additionally, comparisons between experimentally observed and numerically simulated results of temperature field analysis in flow fields have been reported. For example, in one of the studies focused on experimental measurement, Erickson et al. measured the temperature rise due to Joule heating inside a three-dimensional microfluidic device made of poly (dimethylsiloxane) (PDMS) and glass and reported that the results matched the numerical simulations with an accuracy of ±3 °C [28]. Similarly, Williams et al. compared experimental results obtained using the LIF method with numerical simulation results and reported that the temperature rise was proportional to the square of the applied voltage [29].

With respect to the previous studies focused on numerical simulation, Tang et al. proposed a three-dimensional numerical simulation model of thermal fluid flow to investigate the correlation between Joule heating and temperature gradient focusing and reported that the numerical simulation results matched the experimental results well [30]. Rasmussen et al. conducted modeling to optimize flow sensors within microchannels and reported that the simulation results and the temperature field measurements using sensors based on the simulations matched with an error of less than 1% [31]. Many analyses of microflows have been performed using commercial software. Gallo et al. numerically predicted the temperature field due to Joule heating in an insulator-based DEP (iDEP) device [32]. Kwak et al. performed numerical simulations focusing on localized dielectric loss-induced heating in DEP devices and reported that the origin of the heating in DEP devices with electrically insulated electrodes was Debye relaxation [33]. Wang et al. numerically predicted the interactions between electrothermal flow and electroosmotic flow near the constriction region in the microchannel and clarified the temperature rise and flow

field near the constriction [34]. Khoshmanesh et al. analyzed the temperature field in the unique DEP device they developed [35].

In this study, with the aim of studying the effects of high-temperature exposure on cells, the temperature rise in the microchannel of a previously developed eDEP cell separation device was evaluated experimentally and numerically [36]. For the experimental evaluation, the micro-LIF method was adopted to measure the temperature in the device. In the numerical approach, the thermal structure of the device was investigated by performing a numerical simulation in which the effect of heat generation due to a nonuniform electric field was incorporated in the thermofluidic model. Furthermore, parametric numerical simulations were performed with changes in the solution conductivity and sample solution flow rate, which affect cell separation performance. Finally, the correlation between the device operating conditions and temperature rise and their effects on cell viability were explored and discussed.

2. Thermofluidic Numerical Simulation

2.1. Thermofluidic Governing Equations

Figure 1 shows a conceptual diagram of the numerical simulation model. The bottom surface of the microfluidic channel with height $H = 500$ μm consisted of a 400 μm thick glass substrate with counter-interdigitated electrodes printed on it, and the top surface consisted of a 1100 μm thick indium tin oxide (ITO) planar electrode. The length of the microfluidic channel was $L_z = 3600$ μm. Cell separation was performed by generating a nonuniform electric field while sample solution-suspended cells flowed through the microfluidic channel at a constant volumetric flow rate Q.

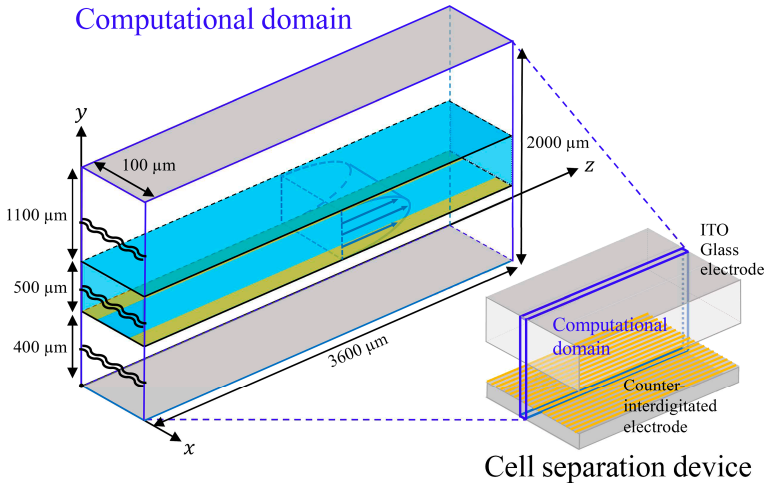


Figure 1. Conceptual diagram of the numerical simulation model.

In the case of analyzing the flow of the electrolyte solution inside the microfluidic channel with the applied A.C. electric field, it was also necessary to evaluate the effects of electroosmotic flow and electrothermal flow near the electrode surfaces on the temperature field, in addition to Joule heating. It is known that the effect of the electroosmotic flow is likely to appear when the electric conductivity of the solution is $\sigma_f \leq 8.4 \times 10^{-2}$ S/m [37]. Ren et al. reported that the order of magnitude of the electroosmotic flow was less than 1.0×10^{-6} m/s under the conditions of an applied voltage $V = 30$ V_{pp} and conductivity $\sigma_f = 1.0 \times 10^{-3}$ S/m [38]. Electrothermal flows have been reported to be more pronounced when high-conductivity solutions ($\sigma_f \sim 0.2$–1.0 S/m) were used [37]. Akutsu et al. reported that the order of magnitude of electrothermal flow was about 7.5×10^{-5} m/s under conditions of an applied voltage $V = 20$ V_{pp} and conductivity $\sigma_f = 2.9 \times 10^{-1}$ S/m [39]. In this study, an applied voltage of $V = 10$ V_{pp} and conductivity of $\sigma_f = 1.0 \times 10^{-3}$–$1.0 \times 10^{-1}$ S/m were adopted. Furthermore, taking into account that the average flow velocity of the sample solution was $U_m \sim 0.5 \times 10^{-3}$ m/s, the effects

of electroosmotic and electrothermal flows on the thermofluidic field in the microchannel could be considered negligible. Regarding the buoyancy effect due to the temperature distribution in the microfluidic channel, the temperature difference in the microfluidic channel, ΔT, was only a few degrees Celsius, and the order of magnitude of the Rayleigh number, Ra, was Ra $\sim$ 100. Therefore, the buoyancy effect could also be considered negligible. The spanwise direction of the microchannel was defined as the x-axis, the height direction as the y-axis, and the flow direction as the z-axis. The sample solution was assumed to be an incompressible homogeneous viscous fluid. A fully developed Poiseuille flow was assumed for the velocity distribution. Thus, the velocity vector of the fluid was given as

$$v = \left(0,\ 0,\ \frac{6Q}{H^3}(H-y)y\right) \tag{1}$$

Here, H is the height of the microfluidic channel, and y is the height from the bottom surface ($0 \leq y \leq H$). Q represents the volumetric flow rate of the sample solution, and it was given using the width of the microfluidic channel, B, as $Q = U_m BH$. The governing equations for the liquid and solid phases in the device are given as

$$\frac{\partial T}{\partial t} + (v \cdot \mathrm{grad})\, T = \frac{\kappa_f}{\rho_f C_{pf}}\left(\frac{\partial^2 T}{\partial x^2} + \frac{\partial^2 T}{\partial y^2} + \frac{\partial^2 T}{\partial z^2}\right) + \frac{q}{\rho_f C_{pf}} \tag{2}$$

$$\frac{\partial T}{\partial t} = \frac{\kappa_g}{\rho_g C_{pg}}\left(\frac{\partial^2 T}{\partial x^2} + \frac{\partial^2 T}{\partial y^2} + \frac{\partial^2 T}{\partial z^2}\right) \tag{3}$$

Here, the values t, κ, ρ, and C_p are time, thermal conductivity, density, and isobaric specific heat, respectively. Subscripts f and g represent fluid and solid, respectively. The second term of the right-hand side of Equation (2) represents heat generation. The Joule heating $q = q(x, y)$ in the electrolyte solution can be given as

$$q = \sigma_f E^2 \tag{4}$$

where σ_f is the electric conductivity of the electrolyte solution and E is the effective value of the electric field.

2.2. Thermofluidic Boundary Conditions

The boundary conditions of the thermofluidic analysis are shown in Figure 2a. The constant temperature boundary condition $T = T_0$ was given for the upstream end of the device ($z = 0$). The freely developed boundary condition of the temperature field was given at the downstream end of the device. The constant wall heat flux condition

$$-\kappa_f \left(\frac{\partial T}{\partial y}\right)_f = -\kappa_g \left(\frac{\partial T}{\partial y}\right)_g \tag{5}$$

was applied to the interface between the liquid and the solid phases in the microfluidic channel. At the top surface of the device, the boundary condition

$$-\kappa_g \left(\frac{\partial T}{\partial y}\right)_g = h_t (T_0 - T_{wt}) \tag{6}$$

was applied. Here, h_t is the convective heat transfer coefficient at the top surface, and T_{wt} is the local temperature at the top surface. h_t was evaluated using the following empirical formula:

$$h_t = \frac{\kappa_a}{L} C_t \mathrm{Ra}_t{}^{\zeta} \tag{7}$$

where L represents the characteristic length of the device and was defined as follows using the perimeter length, l, and area, A, of the electrode substrate:

$$L = \frac{4A}{l} \tag{8}$$

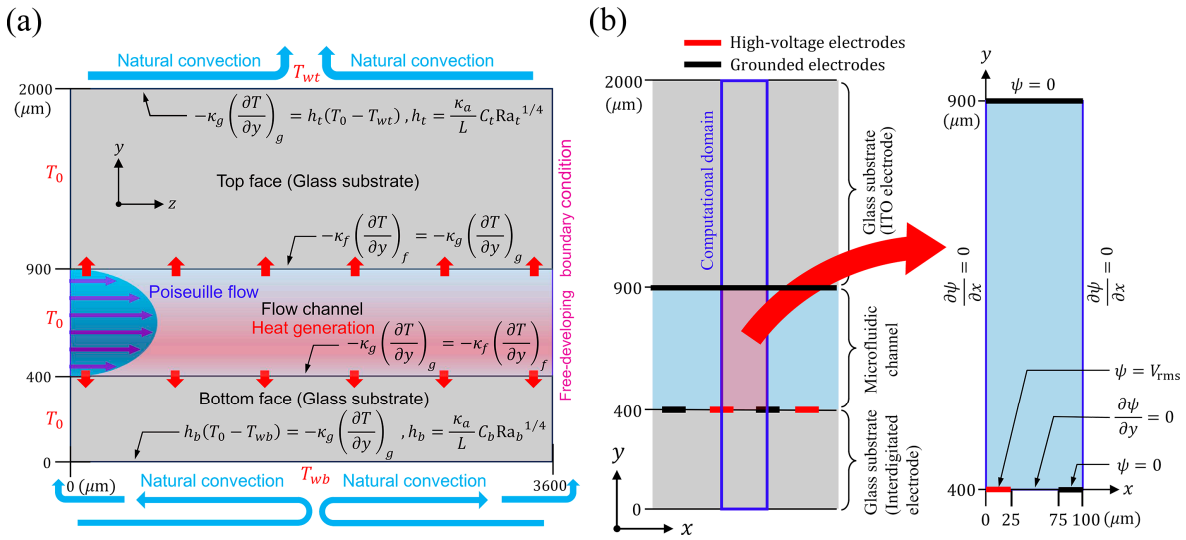


Figure 2. (**a**) Thermofluidic numerical simulation model. (**b**) Electric field analysis model.

The coefficients ζ and C_t were determined empirically. Ra_t is the Rayleigh number at the top surface, defined as

$$\mathrm{Ra}_t = \frac{g\,\beta_a\,(T_0 - T_{wt})\,L^3}{{\nu_a}^2}\mathrm{Pr}_a \tag{9}$$

where the values g, β_a, ν_a, and Pr_a are the gravitational acceleration, thermal expansion coefficient of the air, kinematic viscosity of the air, and Prandtl number of the air, respectively. At the bottom surface of the device, the boundary condition

$$h_b(T_0 - T_{wb}) = -\kappa_g\left(\frac{\partial T}{\partial y}\right)_g \tag{10}$$

was applied. Here, h_b is the convective heat transfer coefficient at the bottom surface, and T_{wb} is the local temperature at the bottom surface. In a similar manner as for h_t in Equation (7), h_b was evaluated using the following empirical formula:

$$h_b = \frac{\kappa_a}{L} C_b \mathrm{Ra}_b{}^{\zeta} \tag{11}$$

Here, Ra_b is the Rayleigh number at the bottom surface, defined as

$$\mathrm{Ra}_b = \frac{g\,\beta_a\,(T_0 - T_{wb})\,L^3}{{\nu_a}^2}\mathrm{Pr}_a \tag{12}$$

The coefficients ζ and C_b were determined empirically. For both lateral faces of the computational domain, the symmetry boundary condition

$$\frac{\partial T}{\partial x} = 0 \tag{13}$$

was applied.

2.3. Governing Equation for Electric Field

The Joule heating per unit time, q, as expressed in Equation (4), is a function of the effective value of the A.C. electric field, E. Therefore, in this study, the electric field in the microchannel was obtained by electrostatic field analysis with E as the dependent variable. Initially, because fingers of the interdigitated electrodes were arranged along the flow direction (z-axis), the electric field in the microfluidic channel could be assumed to be uniform along the flow direction. In other words, the electric field only had a nonuniform distribution within the cross-section of the microfluidic channel. Therefore, the electric field in the microchannel was obtained by solving the Laplace equation for the electrostatic potential, ψ, in the xy-plane of the microchannel:

$$\frac{\partial^2 \psi}{\partial x^2} + \frac{\partial^2 \psi}{\partial y^2} = 0 \tag{14}$$

The electrostatic field E ($|E| = E$) was obtained from the relation

$$E = \left(E_x\ ,\ E_y\right) = \left(-\frac{\partial \psi}{\partial x}, -\frac{\partial \psi}{\partial y}\ \right) \tag{15}$$

using the ψ value obtained by numerically solving Equation (14).

2.4. Boundary Conditions for the Electric Field

Figure 2b shows the electric field analysis model. The computational domain was a part of the microfluidic channel cross-section, including half of a pair of interdigitated electrodes. The boundary conditions for ψ were given as

$$\begin{cases} \psi = V_{\text{rms}} & (\text{High} - \text{voltage electrode}) \\ \psi = 0 & (\text{Grounded electrodes}) \end{cases} \tag{16}$$

The symmetry boundary condition

$$\frac{\partial \psi}{\partial x} = 0 \tag{17}$$

was applied to both lateral faces of the computational domain ($x = 0,\ 100$ μm). The boundary condition

$$\frac{\partial \psi}{\partial y} = 0 \tag{18}$$

was applied to the bottom surface of the microfluidic channel (25 μm $\leq x \leq$ 75 μm, $y = 400$ μm). The boundary condition

$$E_x = 0 \tag{19}$$

was applied to the electrode surfaces and both lateral faces of the computational domain. The boundary condition

$$E_y = 0 \tag{20}$$

was applied to the bottom surface of the microfluidic channel (25 μm $\leq x \leq$ 75 μm, $y = 400$ μm).

2.5. Numerical Simulation Schemes

The governing equations and boundary conditions were discretized using the first-order accurate finite difference scheme in time and the second-order accurate scheme in space. For example, the discretized Equation (3) is denoted as

$$T_{i,j,k}^{n+1} = \alpha_0\ T_{i,j,k}^{n} + \Delta t\left(\alpha_1 T_{i+1,j,k}^{n+1} + \alpha_2 T_{i-1,j,k}^{n+1} + \alpha_3 T_{i,j-1,k}^{n+1} + \alpha_4 T_{i,j+1,k}^{n+1} + \alpha_5 T_{i,j,k-1}^{n+1} + \alpha_6 T_{i,j,k+1}^{n+1}\right) \tag{21}$$

$$\begin{cases} \alpha_0 = 1 + \Delta t \frac{2\kappa_g}{\rho_g C p_g} \left(\frac{1}{\Delta x_i \Delta x_{i-1}} + \frac{1}{\Delta y_j \Delta y_{j-1}} + \frac{1}{\Delta z_k \Delta z_{k-1}} \right) \\ \alpha_1 = \frac{2\kappa_g}{\rho_g C p_g} \frac{1}{\Delta x_i \, (\Delta x_i + \Delta x_{i-1})} \\ \alpha_2 = \frac{2\kappa_g}{\rho_g C p_g} \frac{1}{\Delta x_{i-1} (\Delta x_i + \Delta x_{i-1})} \\ \alpha_3 = \frac{2\kappa_g}{\rho_g C p_g} \frac{1}{\Delta y_j \left(\Delta y_j + \Delta y_{j-1} \right)} \\ \alpha_4 = \frac{2\kappa_g}{\rho_g C p_g} \frac{1}{\Delta y_{j-1} \left(\Delta y_j + \Delta y_{j-1} \right)} \\ \alpha_5 = \frac{2\kappa_g}{\rho_g C p_g} \frac{1}{\Delta z_k \, (\Delta z_k + \Delta z_{k-1})} \\ \alpha_6 = \frac{2\kappa_g}{\rho_g C p_g} \frac{1}{\Delta z_{k-1} (\Delta z_k + \Delta z_{k-1})} \end{cases}$$

where $T^n_{i,j,k}$ is the temperature at grid point (i, j, k) in the computational domain at time $t = n$. Moreover, Δx_i, Δy_j, and Δz_k are the distances to the adjacent grid points in the x, y, and z directions from the grid point (i, j, k), and Δt is the time increment. The convection term in Equation (2) was discretized using the values from the previous time $t = n$.

The computational grid is shown in Figure 3. Note that the number of grid points in the computational grid shown in the figure has been reduced for visibility. A finer grid system was adopted at the channel inlet, the interfaces between the fluid and the glass, and the interfaces between the glass and the air. The number of computational grid points used was $\sim 1,300,000$. This number of computational grids was the minimum number of grids that would not change the results of the simulation. For the heat transfer coefficient h of the horizontal plates corresponding to the upper and lower end surfaces of the device, many empirical formulas have been proposed in the past, and several of these are listed in Table 1. Regarding the exponent ζ of the Rayleigh number Ra in Equations (7) and (11), for the low Rayleigh numbers (Ra $\sim\leq 10^5$), which were relevant to the thermofluidic phenomena targeted in this analysis, a model with $\zeta \sim 1/4$ was proposed. Therefore, in this analysis, a model of $h \sim \mathrm{Ra}^{1/4}$ was also adopted. Regarding the coefficients C_t and C_b appearing in Equations (7) and (11), their magnitudes were generally on the order of 10^{-1} [40–43]. Accordingly, the coefficients C_t and C_b for h_t and h_b were determined as

$$\begin{cases} C_t = 0.1 \\ C_b = 0.1 \end{cases} \tag{22}$$

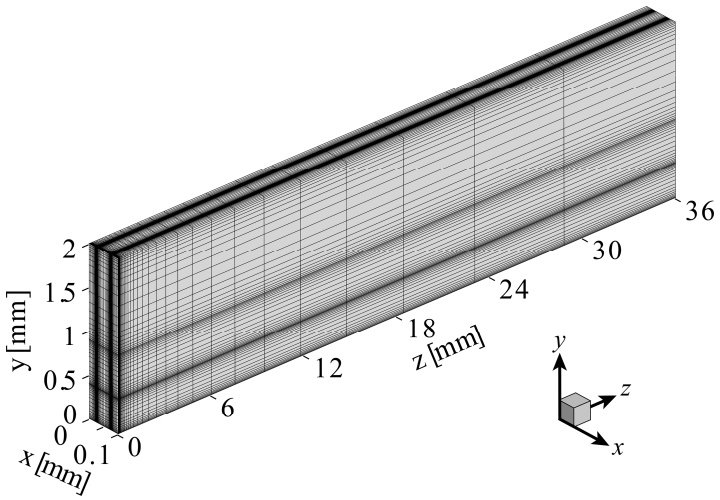


Figure 3. Example of the computational grid.

Table 1. Empirical formulas proposed for the convective heat transfer coefficient h.

Range of Ra	Empirical Formula	Refs.
$10^4 \leq \mathrm{Ra} \leq 10^7$ (Top)	$h = 0.54\mathrm{Ra}^{1/4}$	McAdams et al. [40]
$10^5 \leq \mathrm{Ra} \leq 2 \times 10^7$ (Top) $3 \times 10^5 \leq \mathrm{Ra} \leq 3 \times 10^{10}$ (Bottom)	$h = 0.54\mathrm{Ra}^{1/4}$ $h = 0.27\mathrm{Ra}^{1/4}$	Fishenden et al. [41]
$2 \times 10^5 \leq \mathrm{Ra} \leq 4 \times 10^7$ (Top)	$h = 0.70\mathrm{Ra}^{1/4}$	Al-Arabi et al. [42]
$1 \times 10^2 \leq \mathrm{Ra} \leq 6 \times 10^3$ (Top)	$h = 0.297\mathrm{Ra}^{1/4}$	Yousef et al. [43]

To begin the numerical simulation for thermofluidic analysis, the electric field distribution was solved first using Equations (14)–(20). Then, using Equation (4), the distribution of q in the cross-section of the microfluidic channel was obtained. Next, using Equations (2)–(4), the temperature field in the device was obtained. Time integration was performed with a constant time step until the temperature at the bottom surface of the microfluidic channel became almost constant. The analysis conditions are listed in Table 2. The thermophysical properties used are listed in Table 3. In-house Fortran parallel-computing code managed using OpenMP library was used for the numerical simulations. Computations were performed on the multi-core parallel simulation system of the National Defense Academy.

Table 2. Values of parameters used in the numerical simulation.

Parameters	Values
Number of grid points	$1,300,000$
Time incrementΔt [s]	1.0×10^{-2}
Characteristic length L [m]	6.0×10^{-2}
Characteristic temperature T_0 [K]	293
Effective potential V_{rms} [V]	$5/\sqrt{2}$
Solution conductivity σ_f [S/m]	$1.0 \times 10^{-3} - 1.0 \times 10^{-1}$
Flow rate Q [mL/h]	5.0–50.0

Table 3. Thermophysical properties used in the numerical simulation (20 °C, 1 atm).

	κ [W/(m·K)]	ρ [kg/m^3]	C_p [J/(kg·K)]	ν [m^2/s]	β [1/K]	Pr
Water	6.03×10^{-1}	9.97×10^2	4.19×10^3	1.00×10^{-6}	0.20×10^{-3}	7.01
Air	2.57×10^{-2}	1.17	1.01×10^3	1.50×10^{-6}	3.41×10^{-3}	0.71
Glass	1.05	2.20×10^3	8.40×10^2	—	—	—

3. Experimental

3.1. Device Fabrication

Figure 4a shows the schematic of the electrode substrate. The counter-interdigitated electrode measured 36 mm long and 50 μm wide. The interdigitated electrode used in the experiment was an aluminum film with a thickness of 300 nm fabricated by standard photolithography. In brief, a glass plate measuring 50 mm × 90 mm with a thickness of 0.4 mm was used as the electrode substrate. The plate surface was ultrasonically cleaned using acetone and isopropyl alcohol for 5 min each. A positive photoresist (S1805G; Rohm and Haas Electronic Materials) was spin-coated on the plate surface. The coated plate was baked at 90 °C for 3 min. The resist layer was exposed to UV light through a positive mask image. The exposed photoresist was developed and baked at 130 °C for 3 min. A 300 nm thick layer of the aluminum was vacuum-deposited over the plate. The uncovered aluminum area was etched with mixed acid at 40 °C for 90 s. Finally, the photoresist was removed using an AZ 100 remover (AZ Electronic Materials). Figure 4b shows the components of the cell separation device. The upper surface was a glass substrate with a

thickness of 1.1 mm coated with ITO film. It had ϕ1.0 holes for introducing and draining the cell sample solution, which were made using a router (2307396; Sea Force). Polypropylene female Luer fittings were adhered to the perforated parts, and lead wires were attached to the electrode terminals using conductive epoxy adhesive. A microfluidic channel of dimensions 0.5 mm (H) × 36 mm (L_z) × 10 mm (B) was constructed with parallel top and bottom glass plates separated by 0.5 mm with a silicon rubber spacer.

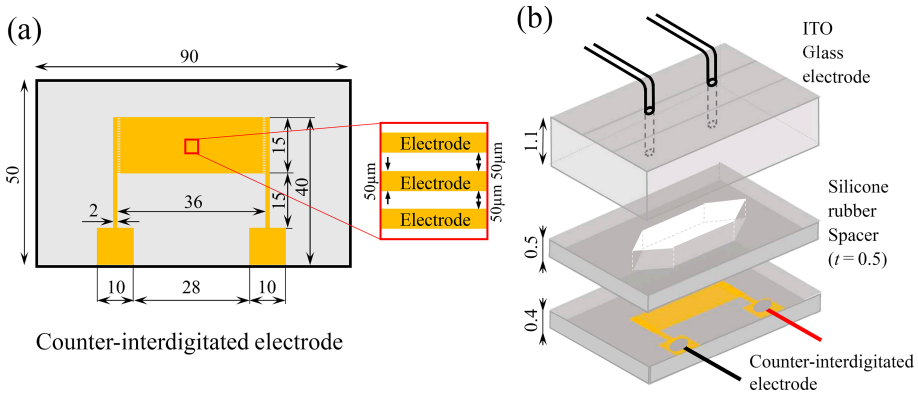


Figure 4. (**a**) Schematic of the electrode substrate. (**b**) Conceptual diagram of the components of the cell separation device.

3.2. Sample Solution Preparation

Rhodamine B (Sigma 83695-250MG; ex. 553 nm, em. 627 nm) was used as the fluorescent dye. A 300 mM mannitol solution was used as the solvent.

3.3. Experimental Setup

Figure 5 shows the schematic diagram of the main part of the experimental apparatus. The experimental apparatus is almost the same as the apparatus used in the cell separation experiment [36]. The width B and length X of the microfluidic channel were $B = 10$ mm and $X = 36$ mm, respectively. The temperature of the sample solution was measured with a T-type thermocouple. A 5 mL volume of sample solution was introduced into the microfluidic channel at a constant flow rate using a syringe pump, and an AC voltage of $V = 10$ V_{pp} was applied to the device. A laser beam with an excitation wavelength of 559 nm and a bandpass filter with a wavelength range of 570–670 nm were used to acquire fluorescence images. Acquisition of a reference image for image division and measurement of the initial temperature were performed prior to applying the AC voltage to the device. Fluorescence image acquisition was performed every 30 s from the onset of the voltage application ($t = 0$) until $t = 1500$ s elapsed. The experimental conditions are listed in Table 4.

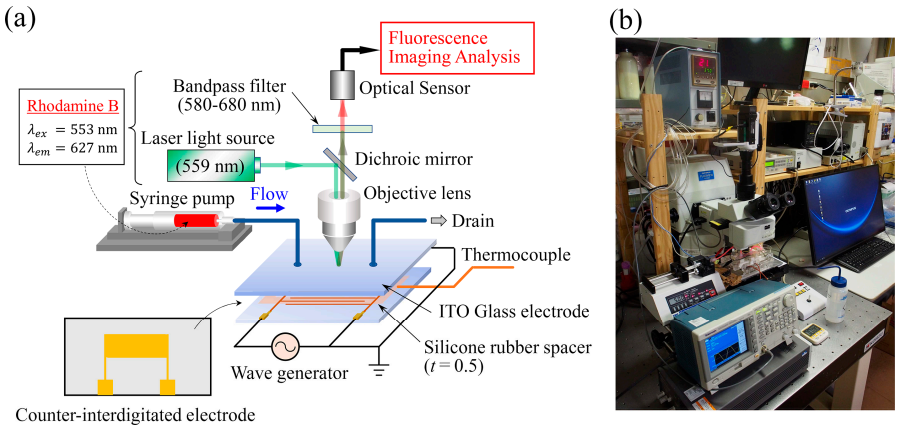


Figure 5. (**a**) Schematic diagram of the primary part of the experimental setup. (**b**) Snapshot of the experimental setup.

Table 4. Experimental conditions.

Parameters	Values
Applied voltage V $[V_{pp}]$	10
Rhodamine B solution [μM]	20
Solution conductivity σ_f [S/m]	4.0×10^{-2}
Frequency f [kHz]	57.6
Flow rate Q [mL/h]	5

3.4. Image Processing

Figure 6 shows the procedure for converting the acquired fluorescence image into images of the distribution of temperature rise ΔT. ImageJ "https://imagej.nih.gov/ij/" (accessed on 1 November 2024) was used for image analysis. The time-lapse fluorescence images were sequentially read by ImageJ and divided by the reference image to produce images of the ratio of the fluorescence intensity. Values of the ratio of fluorescence intensity were converted into ΔT values using a calibration curve of temperature and fluorescence intensity ratio to obtain a pseudocolor temperature distribution. The mean value of ΔT at each elapsed time was obtained from the distribution of histograms of ΔT after temperature transformation, using Python3 (ver. 3.9.6) code.

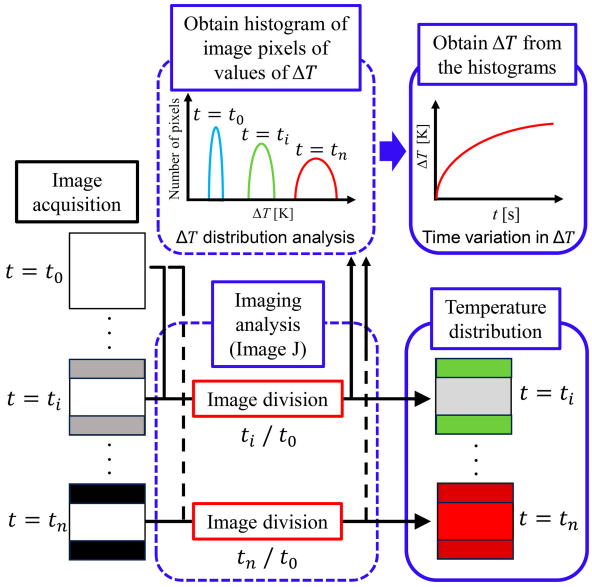


Figure 6. Procedure of the imaging analysis.

3.5. Temperature Calibration

Calibration of the temperature against the fluorescence intensity ratio was performed using a plate reader (DTX-880; Beckman Coulter). The temperature in the chamber of the plate reader was changed every 5 °C from 25 °C to 45 °C to acquire the fluorescence intensity. The calibration curve obtained is shown in Figure 7a. The calibration curve was normalized to that at a temperature of 25 °C. The histogram obtained by imaging analysis is shown in Figure 7a. The average values of ΔT was defined as

$$\Delta T = \frac{\sum_{p=1}^{M} \Delta T_p \cdot k\left(\Delta T_p\right)}{\sum_{p=1}^{M} k\left(\Delta T_p\right)} \tag{23}$$

where ΔT_p is the temperature rise of the p-th image pixel, k is the number of image pixels having the value of ΔT_p, and M is the largest number of pixels. The resolution of the temperature rise was $\Delta T_p - \Delta T_{p-1} = 0.26$ °C.

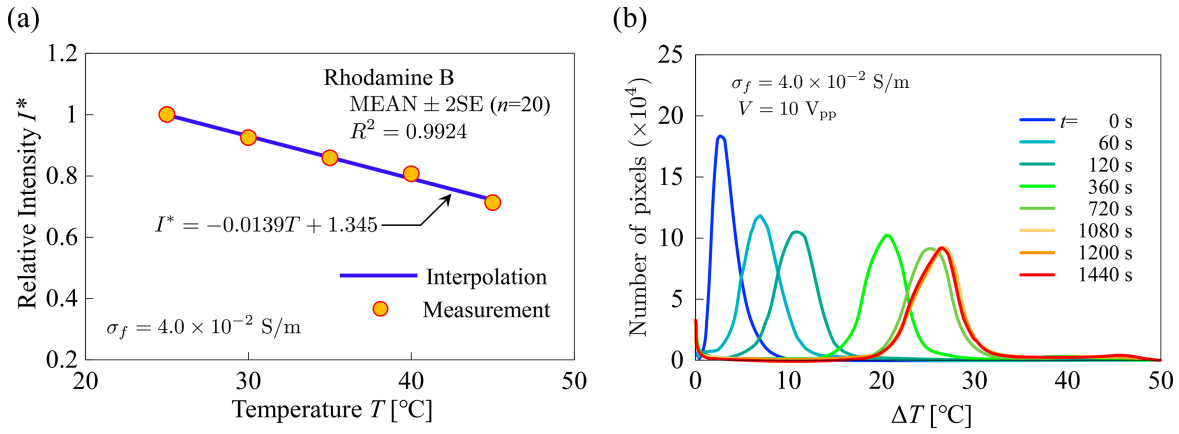


Figure 7. (**a**) Temperature calibration curve. (**b**) Histogram obtained by imaging analysis.

4. Results and Discussion

4.1. Developed Code Verification

4.1.1. Developed Code Verification

Figure 8a shows the distribution of (left) the electrostatic potential, $\psi*$, and (right) the electric field, $E*$, in the cross section of the microfluidic channel. The potential and electric field are non-dimensionalized as $\psi* = \psi / V_{\mathrm{rms}}$ and $E* = EH / V_{\mathrm{rms}}$, respectively. The color contours represent the results using the developed simulation code, and dashed monochrome lines represent the results using the commercial software FEATool Multiphysics "https://www.featool.com/multiphysics/" (accessed on 1 November 2024). The number of grid points used in the commercial software was 2.6×10^6. The convergence criterion of the relative error of the iterative calculation was defined as $<1.0 \times 10^{-8}$. As shown in Figure 8a, the electric field was extremely strong in the vicinity of the electrode edges. Thus, the strong electric field, which is highly localized in the microfluidic channel, acts as a strong local heat source. Therefore, it is essential to ensure sufficient spatial resolution in this region to accurately evaluate the temperature field. The electric field obtained by the developed simulation code was in good agreement with that obtained by the commercial software, confirming that the developed simulation code has sufficient accuracy. Figure 8b shows the profile of the local Nusselt number for parallel-plate laminar flow of isothermal walls obtained with the developed simulation code, compared with those reported by Shah and London [44]. The boundary conditions are constant wall temperature ($T = 23$ °C) and constant inflow temperature ($T = T_0$). The dimensionless z-coordinate is defined as

$$z^* = \frac{z}{2H\mathrm{Re} \cdot \mathrm{Pr}} \tag{24}$$

$$\mathrm{Re} = \frac{2HU_m}{v_f} \tag{25}$$

and calculations were performed under the condition of $\mathrm{Re} = 400$. The local Nusselt number is defined as

$$\mathrm{Nu}_{z^*} = \frac{2H}{T_\mathrm{w}(z^*) - T_\mathrm{b}(z^*)} \left(-\frac{\partial T(z^*)}{\partial y} \right)_{y=0} \tag{26}$$

where T_w is the temperature at the bottom surface of the microfluidic channel and T_b is the bulk mean temperature of the fluid defined as

$$T_\mathrm{b} = \frac{\int_S \rho_f C_{pf}\, T(x,y,z^*)\, w dS}{\int_S \rho_f C_{pf}\, w dS} \tag{27}$$

where S represents the cross-sectional area of the microfluidic channel in the computational domain. The values of Nu_{z^*} obtained by the developed simulation code were in good agreement with that obtained in the previous study, confirming that the developed thermofluidic simulation code has sufficient accuracy.

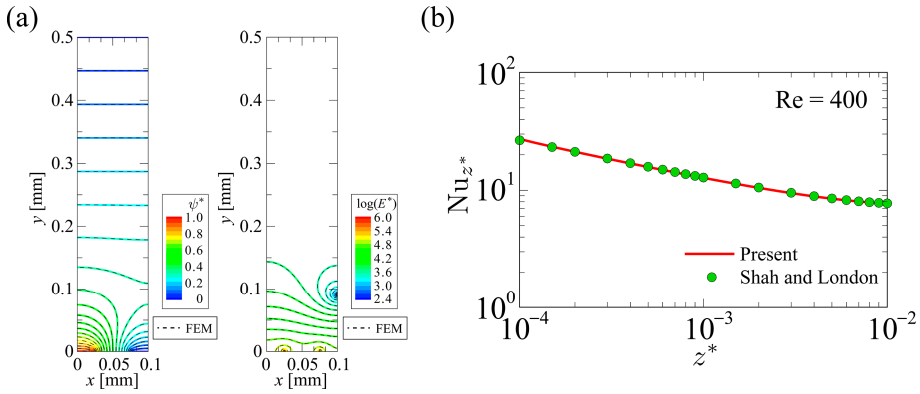


Figure 8. (**a**) Distributions of (left) electric potential and (right) electric field. (**b**) Local Nusselt number for isothermal wall.

4.1.2. Thermal Structure of the Device

Figure 9 shows the transient of the distribution of temperature rise, ΔT ($= T - T_0$), in the computational domain. The analysis conditions were set to $\sigma = 4.0 \times 10^{-2}$ S/m and $Q = 5.0$ mL/h to match the experimental conditions of the developed cell separation device [36]. Numerical simulation was performed until $t = 1440$ s when the cell separation of 2 mL of sample solution was completed in the experiment. ΔT reached its maximum value at the bottom of the microfluidic channel, where the generation of Joule heat was the greatest. The temperature distribution had a gradual increase along the flow direction (z) across the liquid phase (microfluidic channel) and solid phases (top and bottom glass substrates). The results imply that heat transport by diffusion is dominant over that by convection in the device. The maximum of ΔT appeared at the downstream end of the microfluidic channel, which was predicted to reach ~ 21 °C at time $t = 1440$ s.

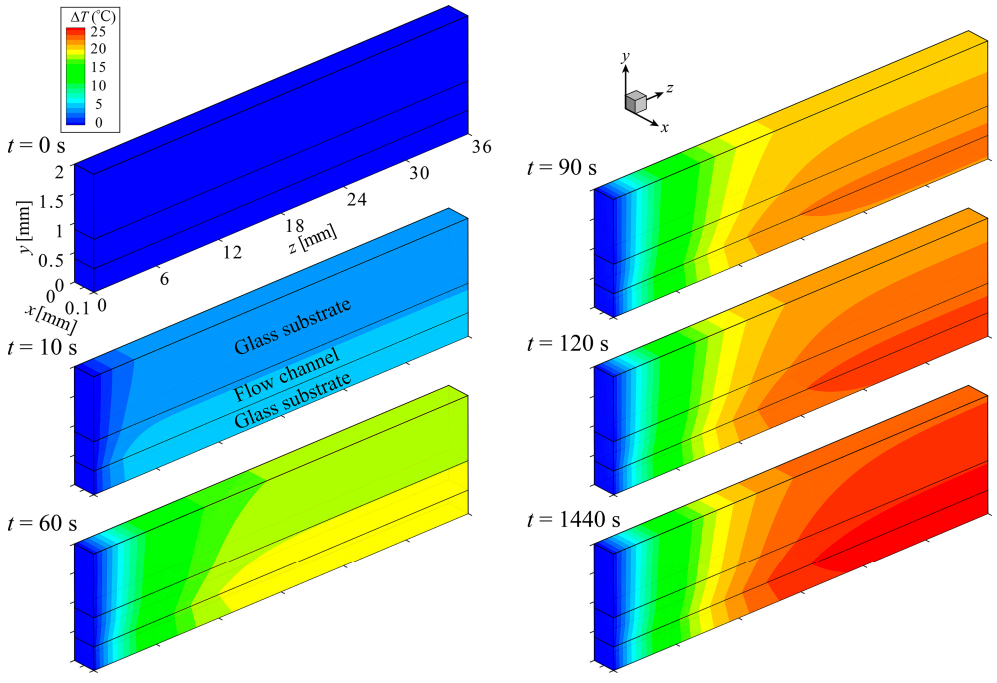


Figure 9. Transient of the temperature-rise distribution in the computational domain. ($\sigma = 4 \times 10^{-2}$ S/m, $Q = 5.0$ mL/h).

Figure 10 shows the time variations of the distributions of (a) the temperature rise at the bottom surface of the microfluidic channel, ΔT_w ($= T_w - T_0$), along the flow direction, and (b) the local Nusselt number, Nu, along the flow direction, up to $t = 1500$ s, for $\sigma = 1.0 \times 10^{-2}$ S/m and $Q = 10.0$ mL/h. Nu is defined as

$$\mathrm{Nu} = -\frac{2H}{T_w(z) - T_b(z)} \left(-\frac{\partial T(z)}{\partial y} \right)_{y=0} \tag{28}$$

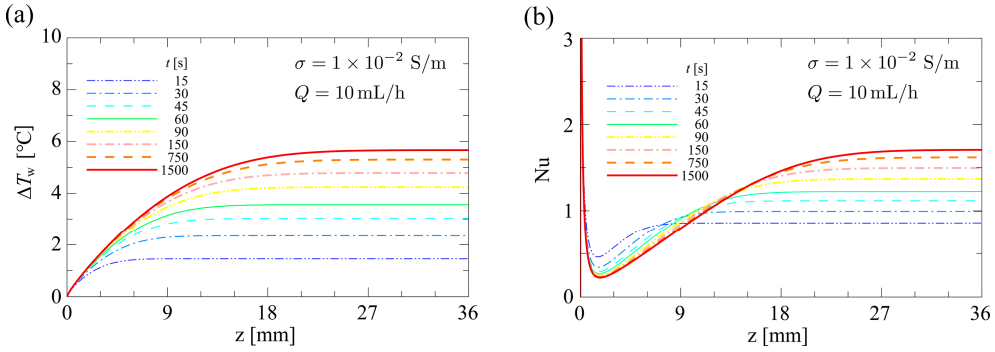


Figure 10. Time variations of the distributions of (**a**) the temperature rise at the bottom surface of the microfluidic channel and (**b**) the local Nusselt number.

Here, T_w and $\partial T(z)/\partial y$ are the values of the local temperature and temperature gradient at the bottom of the microfluidic channel, averaged with respect to the span direction.

$$T_w(z) = \frac{\int T_w(x,0,z)dx}{\int dx}, \quad \left(\frac{\partial T(z)}{\partial y} \right)_{y=0} = \frac{\int (\partial T(x,y,z)/\partial y)_{y=0} dx}{\int dx} \tag{29}$$

Unless otherwise specified, all distributions of thermophysical quantities in the flow direction represent the spanwise averaged distribution. As shown in Figure 10a, because the Joule heat was generated almost uniformly along the flow direction over the bottom surface of the microfluidic channel, ΔT_w began to increase uniformly in the flow direction as soon as the voltage was applied. On the other hand, the upstream end of the microfluidic channel was cooled by the inflow fluid. Therefore, while ΔT_w increased uniformly with time, a distribution was presented in which the high-temperature plateau gradually narrowed from the upstream side due to the cooling effect of the convection heat transport of the inflow fluid. As shown in Figure 10b, the area near the inlet of the microfluidic channel, $T_w - T_b$, presented its maximum value due to Joule heating, and the Nusselt number, Nu, presented its minimum value. On the other hand, T_b did not increase because the area near the inlet continued to be cooled. Therefore, the minima of Nu became even smaller as time passed. On the downstream side of the microfluidic channel, Nu gradually increased uniformly due to Joule heating. Compared to the distribution of Nu shown in Figure 8b, which was obtained under the condition of constant wall temperature, the distribution obtained in this study was different. In the thermofluidic field under study, the fluid in the microfluidic channel was found to be heated spatially nonuniformly by Joule heating due to the presence of the nonuniform electric field. These are the characteristics of the temperature field within the cell separation device.

This analysis did not take into account the presence of cells in the microfluidic channel. No quantitative assessment has been reported regarding the potential impact of cells present in the solution on the temperature generated by DEP. Given that 60–70% of a cell's composition is water, it is expected that the thermal properties of cells will not significantly deviate from those of the solution. Therefore, it is considered unlikely that the presence of cells in the solution will affect the surrounding thermal environment. On the other hand, when selecting a solvent, the solvent should have the property of mitigating the temperature rise in the microchannel. For example, certain organic solvents or oils have

been reported to have a solution conductivity $\sigma_f = 10^{-6}$–10^{-10} S/m at 20 °C, which is expected to help mitigate temperature rise due to Joule heating. However, cautious discussion is necessary when considering the use of these types of solutions, as they may pose various concerns regarding potential impacts on the physiological functions of cells.

4.1.3. Influence of Flow Rate and Conductivity on Temperature

Figure 11 shows (top) the distribution of the local temperature rise at the bottom surface of the microfluidic channel, ΔT_w, along the flow direction and (bottom) the time variation of the mean temperature rise, ΔT_{wm}, for varying σ and Q. ΔT_{wm} is defined as

$$\Delta T_{wm}(t) = \frac{\int \Delta T_w(t) dz}{\int dz} \tag{30}$$

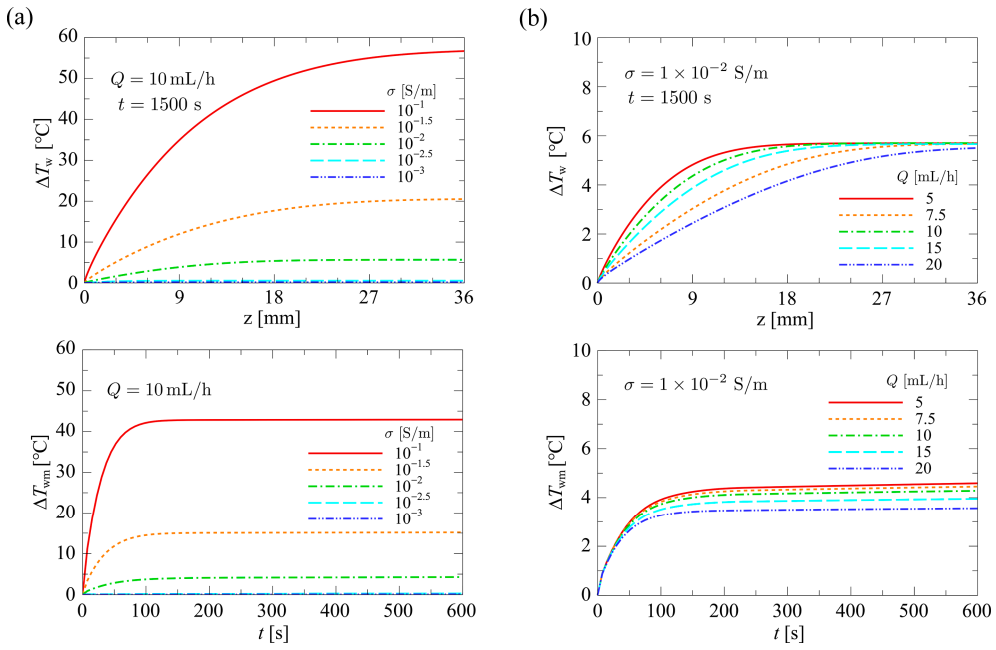


Figure 11. (**a**) σ dependence of (top) the distribution of the temperature rise and (**bottom**) the time variation of the mean temperature rise. (**b**) Q dependence of (**top**) the distribution of the temperature rise and (bottom) the time variation of the mean temperature rise.

For ΔT_w, the distribution for the thermal steady state ($t = 1500$ s) is shown, and for ΔT_{wm}, the transient variation is shown up to $t = 600$ s, when the value changed significantly. In Figure 11a, Q was fixed at $Q = 10.0$ mL/h, and σ was varied in the range $\sigma = 1.0 \times 10^{-3}$–$1.0 \times 10^{-1}$ S/m. In Figure 11b, σ was fixed at $\sigma = 1.0 \times 10^{-2}$ S/m, and Q was varied in the range $Q = 5.0$–20.0 mL/h. As shown in the top panel of Figure 11a, the distribution of ΔT_w increased proportionally with σ. This is because the heat generation term q on the right-hand side of Equation (4) is proportional to σ. As shown in the top panel of Figure 11b, the effect of convective heat transfer became significant with increasing Q, and the shape of the ΔT_w profile transitioned from a parabolic form to a linear form. From the above, it was found that Q is the dominant parameter for the shape of the distribution of ΔT_w in the microfluidic channel. Therefore, in order to maintain a uniform temperature distribution in the microfluidic channel, which is desirable for cell separation devices, it is essential to minimize the value of Q as much as possible. In this study, the heat exchange by conduction was not considered as a thermal boundary condition at the downstream end of the device. Therefore, under actual cell separation operations, the temperature at the downstream end of the device is expected to be affected by the external thermal environment at the downstream end of the device.

Figure 12 shows a bird's-eye view of ΔT_{wm} as a function of both σ and Q after the temperature field reached a steady state. Parametric calculations ($\sim$ 200 simulations) were performed with σ varying in the range of $\sigma = 1.0 \times 10^{-3}$–$1.0 \times 10^{-1}$ S/m, and Q in the range of $Q = 5.0$–50.0 mL/h. As shown in Figure 12, the value of ΔT_{wm} changed rapidly in the range of $\sigma = 1.0 \times 10^{-2}$–$1.0 \times 10^{-1}$ S/m regardless of the value of Q. Moreover, at higher values of σ, it was found that the value of ΔT_{wm} varied significantly with variations in Q. Under these conditions, the effect of convective heat transport on the temperature rise was pronounced due to the high heat generation, resulting in a distinct Q-dependence of ΔT_{wm}. The maximum value of ΔT_{wm} reached approximately 48 °C. Elengoe et al. reported that the viability of MCF10A and MDA-MB-231 cells was decreased by exposure to a 41 °C environment for 30 min [45]. Furthermore, it has been reported that exposure to high-temperature environments induces adverse effects on cells, including cell death and reduced viability [19–21]. Therefore, the highest value of the predicted ΔT_{wm} is considered to have a non-negligible influence on cells during the cell separation process.

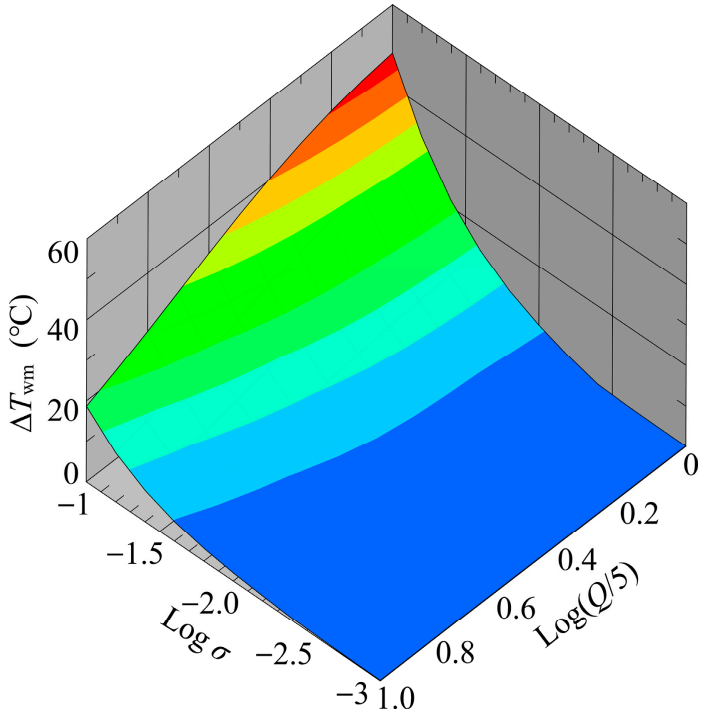


Figure 12. Variation of the mean temperature rise with respect to variations of flow rate and conductivity.

4.1.4. Influence of Flow Rate and Conductivity on the Nusselt Number

Figure 13 shows (top) the distribution of the local Nusselt number at the bottom surface of the microfluidic channel, Nu, along the flow direction and (bottom) the time variation of the mean Nusselt number, Nu_m, for varying σ and Q. Nu_m is defined as

$$Nu_m(t) = \frac{\int Nu(t)dz}{\int dz} \tag{31}$$

For Nu, the distribution for the thermal steady state ($t = 1500$ s) is shown, and for Nu_m, the transient variation is shown up to $t = 600$ s, when the value changed significantly. In Figure 13a, Q was fixed at $Q = 10.0$ mL/h, and σ was varied in the range of $\sigma = 1.0 \times 10^{-3}$–$1.0 \times 10^{-1}$ S/m. In Figure 13b, σ was fixed at $\sigma = 1.0 \times 10^{-2}$ S/m, and Q was varied in the range of $Q = 5.0 \sim 20.0$ mL/h. As shown in the top panel of Figure 13a, the distribution of Nu exhibited its minimum value near the inlet of the microfluidic channel regardless of the value of σ. Then, due to the heat balance between Joule heating and heat diffusion from the bottom surface of the microfluidic channel, Nu gradually increased along the

flow and eventually asymptotically approached a constant value. The position from the inlet of the microfluidic channel where Nu asymptotically approached a constant value moved downstream in proportion to the value of σ, i.e., the amount of heat generated. In other words, the value of z at which the temperature field reaches thermal equilibrium shifted downstream as σ increased. In the bottom panel of Figure 13a, for a large value of σ, $\mathrm{Nu_m}$ exhibited a minimum value for a short while ($<\sim$ 20 s) after the onset of the voltage application. This is because, in cases of large heat generation, the T_b was initially low, resulting in a large $T_\mathrm{w} - T_\mathrm{b}$ near the inlet. As the temperature rose, heat dissipation from the bottom surface of the microfluidic channel increased, causing $\mathrm{Nu_m}$ to gradually increase and eventually reach a constant value when the device reached thermal equilibrium. The top panel of Figure 13b shows the dependence of the Nu distribution on Q. As the value of Q increased, the value of Nu decreased. This is because the temperature rise in the microfluidic channel was suppressed due to the inflow of fluid at room temperature from the inlet. In this study, heat conduction at the downstream end of the microfluidic channel is not considered in the thermal boundary condition. Therefore, $\mathrm{Nu_m}$ decreased simply in accordance with the increase in Q as shown in the bottom panel of Figure 13b. The convective heat transport due to the increase in Q would suppress the temperature rise in the microfluidic channel.

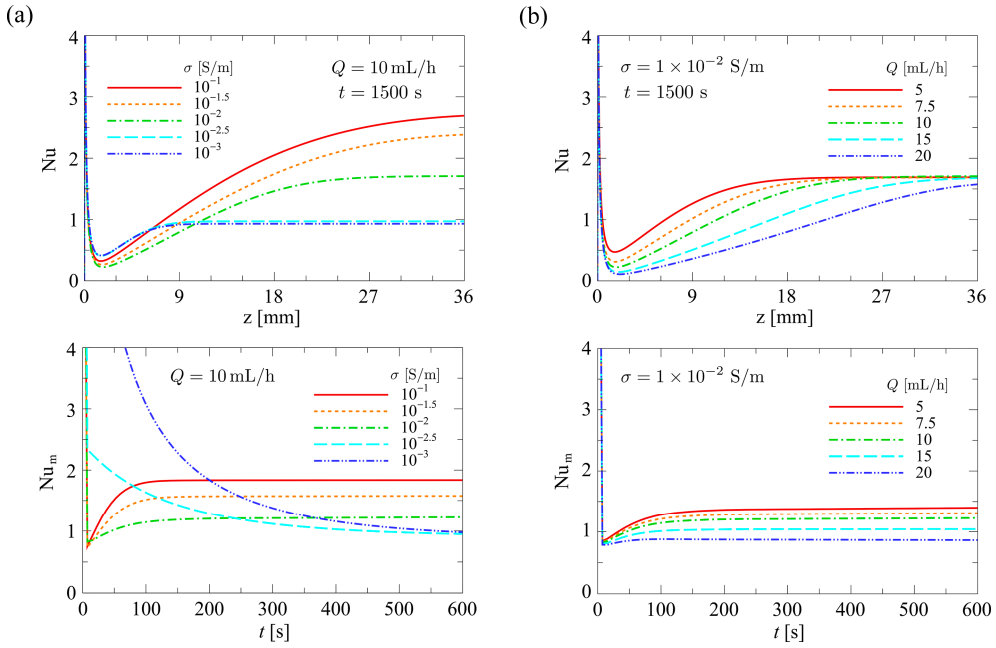


Figure 13. (**a**) σ dependence of (top) the distribution of the Nusselt number and (**bottom**) the time variation of the mean Nusselt number. (**b**) Q dependence of (**top**) the distribution of the Nusselt number and (bottom) the time variation of the mean Nusselt number.

Figure 14 shows a bird's-eye view of $\mathrm{Nu_m}$ as a function of both σ and Q after the temperature field reached a thermal steady state. In the range of $\sigma = 1.0 \times 10^{-2.2}$–$1.0 \times 10^{-1}$ S/m, $\mathrm{Nu_m}$ transitioned smoothly with changes in Q, while in the range of $\sigma = 1.0 \times 10^{-3}$–$1.0 \times 10^{-2.2}$ S/m, $\mathrm{Nu_m}$ remained nearly flat regardless of the value of Q. The maximum value of $\mathrm{Nu_m}$ appeared when σ was at its maximum and Q was at its minimum, while the minimum value of $\mathrm{Nu_m}$ appeared when $\sigma = 1.0 \times 10^{-2.2}$ and $Q = 50.0$ mL/h. The results suggest that $\sigma \sim 1.0 \times 10^{-2.2}$ S/m may be the threshold for a significant change in the thermal structure in the microfluidic channel of the present cell separation device.

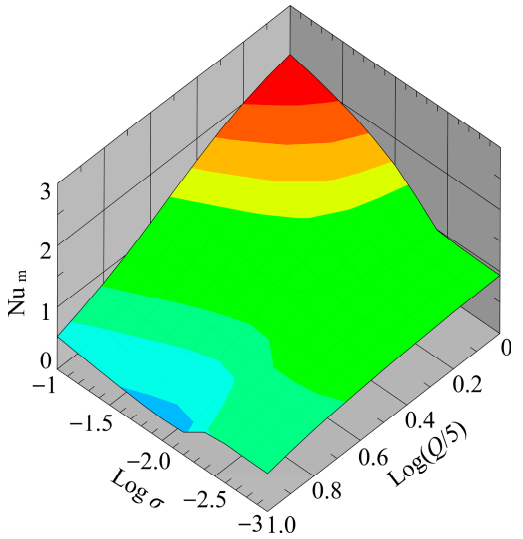


Figure 14. Variation of the mean Nusselt number with respect to variations in flow rate and electric conductivity.

4.2. Experimental Results and Comparison with Numerical Simulation

Figure 15 shows the transient of the distribution of the temperature rise, ΔT, at the bottom surface of the microfluidic channel within a 100 μm × 100 μm area in the center of the device, displayed in pseudocolor. The top panel represents the numerical simulation results, and the bottom panel represents the experimental results. In the numerical simulation, ΔT increased significantly until $t \cong 120$ s, after which it hardly increased at all. In contrast, the experimental results showed a gradual increase in ΔT up to $t \cong 1440$ s. Moreover, the experimental results showed some temperature difference between the electrode and glass substrate, whereas the simulation results showed uniform ΔT distributions. This difference may be attributable to the fact that the numerical simulation model ignored the thickness of the metal electrode (300 nm). The difference in heat capacity between the metal and glass may be responsible for the difference in the rate of temperature rise. However, since heat transport by conduction was dominant in the microfluidic channels, there was actually little temperature difference between the electrode surface and the glass surface, as shown in the experimental results. Figure 16 shows the transient of the averaged ΔT with respect to the 100 μm × 100 μm area in the center of the bottom surface of the microfluidic channel, comparing the experimental and numerical simulation results. In the experiment, as can be seen from the transient behavior of ΔT in Figure 16, the temperature field in the device nearly reached a steady state at $t \cong 720$ s, whereas in the numerical simulation, it reached a steady state at $t \cong 240$ s. The difference in the time history of ΔT between the two may be due to the fact that the numerical simulation did not take into account the effect of heat dissipation from both lateral sides of the device (relative to the flow direction). To evaluate the impact of heat loss from both sides of the device, numerical simulations using a model that isolates the side portions of the device may be considered. Additionally, adopting a model that accounts for heat conduction at the downstream end of the device is expected to allow a more accurate assessment of the temperature profile. Alternatively, simulations using a bulk model that ignores the interdigitated electrode structure may be considered as a more practical option. Another factor to consider is the validity of the values of h_b and h_t. In this study, the values of h_b and h_t were estimated using reasonable empirical formulas that took into account the length scales under analysis and were roughly of the order of magnitude of 2–3 digits [46]. On the other hand, in previous reports on numerical simulation of Joule heating within microfluidic channels [23,24], the value of the heat transfer coefficient h was significantly higher than what is typically expected from natural convection of air, covering a range of 20–20,000 W/(m^2·K). A value of $h \sim 20,000$ W/(m^2·K) is on the same order of magnitude as that observed in boiling heat transport phenomena. The setting of various

parameter values used for boundary conditions could potentially have a non-negligible effect on the evaluation of the temperature field. Nakano et al. [24] have pointed out that the results of temperature field analysis through numerical simulation largely depend on the determination of h values. In modeling for thermofluidic analysis, it is believed that physically reasonable assumptions are crucial for constructing models that contribute to the accurate understanding of phenomena. Regarding the accuracy and error assessment of the micro-LIF method, a previous study has shown that an error of approximately $\pm$ 2 °C can occur at a 95% confidence level [47]. In the present study, the measurement error was approximately $\pm$ 2.5 °C up to t = 720 s as shown in Figure 16. It was also confirmed that measurement error increased over time, which is thought to be attributable to electrode degradation caused by prolonged high electric field application. This effect would be mitigated by reducing the applied field intensity and the duration of application. Therefore, the measurement error is expected to decrease even when the temperature differentials are small. The other factors contributing to error include the fluctuations in the luminance of the laser sheet due to the scanning of the laser beam and intensity noise, which are expected to result in greater measurement errors compared to conventional LIF methods. Systematic error evaluation of the micro-LIF method in this study is challenging. However, with the introduction of methods such as the two-color LIF technique, more accurate measurements may be achievable in the future. The impact of measurement temperature error could have non-negligible adverse effects on the physiological functions of cells if, for instance, there is a 2 °C increase from the average experimental result. This is because even a few degrees of variation in a high-temperature environment above 40 °C can induce significant adverse effects on cellular physiological functions.

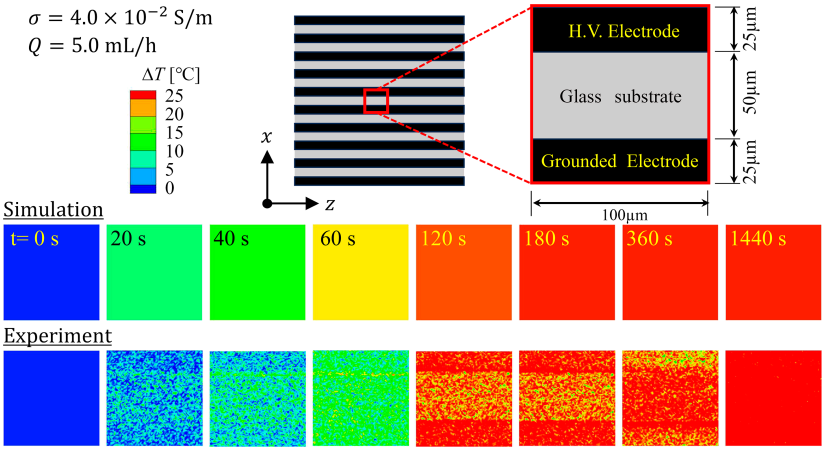


Figure 15. Transient of the temperature-rise distribution at the bottom surface of the microfluidic channel. Numerical simulation results (**top**) and experimental results (**bottom**).

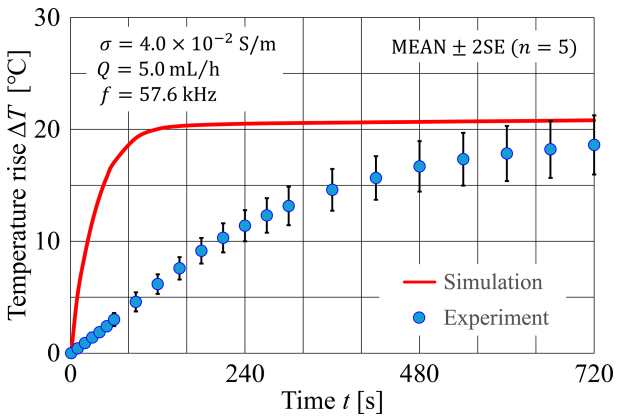


Figure 16. Time variation of the average temperature rise at the bottom of the microfluidic channel.

5. Conclusions

In recent years, dielectrophoresis-based cell separation technologies have attracted attention as a method that is noninvasive to cells. On the other hand, there are concerns about the effects of the high-temperature environment inside the device caused by Joule heating due to the strong electric field on the physiological functions of cells. In this study, we investigated the temperature field inside the microfluidic channels of a previously developed cell separation device through both experimental and numerical approaches. In the experiment, the micro-LIF method was adopted to measure the temperature in the device. In the numerical approach, the thermal structure of the device was investigated by performing a numerical simulation in which the effect of heat generation due to a nonuniform electric field was considered in the model. The experimental results revealed that the temperature rise at the bottom surface of the microfluidic channel was approximately 20 °C after 1440 s of voltage application. The transient of the thermofluidic phenomena in the device was investigated by numerical simulation, and an attempt was made to elucidate the thermal structure of the device. Additionally, a parametric analysis was conducted to investigate the correlation between the flow rate of the cell sample solution or the solution conductivity and the temperature field. The results suggested that, under certain operational conditions, the temperature rise from room temperature could exceed 40 °C. Our findings suggested that under certain operating conditions, the device could significantly affect the physiological functions of cells. Due to the structure of the proposed device, electric field lines concentrate at the edges of the electrodes. Since the solution near this region acts as a heat source, it may be challenging to reduce the heat generation itself. Moreover, considering the thermal transport characteristics at the microscale, attempts to mitigate the overall temperature increase of the device may be effective, as heat generated within the microchannel diffuses efficiently throughout the device. Methods to suppress the temperature rise of devices include using metal, which has higher thermal conductivity than glass, as the material for the device's upper electrode plate and inducing forced convection of air on the substrate surface. It is believed that these approaches enhance the heat dissipation of the device. Additionally, leveraging the microscale advantage to further miniaturize the device may enhance heat transfer. However, verifying these effects is challenging, as measuring temperature within microchannels by methods other than optical techniques, such as LIF methods, is extremely difficult. Thus, at present, accurately predicting the temperature rise may rely solely on high-precision numerical simulations. To achieve both an improvement in device performance and a reduction in stress for the cells, detailed exploration of the optimal operating conditions is indispensable.

Author Contributions: Conceptualization, Y.S. and S.T.; methodology, Y.S. and S.T.; software, Y.S. and S.T.; validation, Y.S. and S.T.; formal analysis, Y.S. and S.T.; investigation, Y.S. and S.T.; resources, S.T.; data curation, Y.S. and S.T.; writing—original draft preparation, Y.S.; writing—review and editing, S.T.; visualization, Y.S. and S.T.; supervision, S.T.; project administration, S.T.; funding acquisition, S.T. All authors have read and agreed to the published version of the manuscript.

Funding: This work was supported by JSPS KAKENHI Grant Number JP23K03669.

Institutional Review Board Statement: Not applicable.

Informed Consent Statement: Not applicable.

Data Availability Statement: Data will be provided on reasonable request.

Acknowledgments: Numerical simulations were performed on the multi-core parallel simulation system of the National Defense Academy.

Conflicts of Interest: The authors declare no conflicts of interest.

References

1. Mustafa, A.; Pedone, E.; Marucci, L.; Moschou, D.; Di Lorenzo, M. A flow-through microfluidic chip for continuous dielectrophoretic separation of viable and non-viable human T-cells. *Electrophoresis* **2022**, *43*, 501–508. [CrossRef] [PubMed]

2. Puri, P.; Kumar, V.; Belgamwar, S.U.; Ananthasubramanian, M.; Sharma, N.N. Microfluidic platform for dielectrophoretic separation of bio-particles using serpentine microelectrodes. *Microsyst. Technol.* **2019**, *25*, 2813–2820. [CrossRef]
3. Yildizhan, Y.; Erdem, N.; Islam, M.; Martinez-Duarte, R.; Elitas, M. Dielectrophoretic separation of live and dead monocytes using 3D carbon-electrodes. *Sensors* **2017**, *17*, 2691. [CrossRef] [PubMed]
4. Jones, T.B. Basic theory of dielectrophoresis and electrorotation. *IEEE Eng. Med. Biol. Mag.* **2003**, *22*, 33–42. [CrossRef]
5. Aghaamoo, M.; Aghilinejad, A.; Chen, X.L.; Xu, J. On the design of deterministic dielectrophoresis for continuous separation of circulating tumor cells from peripheral blood cells. *Electrophoresis* **2019**, *40*, 1486–1493. [CrossRef]
6. Ayala-Mar, S.; Perez-Gonzalez, V.H.; Mata-Gomez, M.A.; Gallo-Villanueva, R.C.; Gonzalez-Valdez, J. Electrokinetically driven exosome separation and concentration using dielectrophoretic-enhanced PDMS-based microfluidics. *Anal. Chem.* **2019**, *91*, 14975–14982. [CrossRef]
7. Jiang, A.Y.L.; Yale, A.R.; Aghaamoo, M.; Lee, D.H.; Lee, A.P.; Adams, T.N.G.; Flanagan, L.A. High-throughput continuous dielectrophoretic separation of neural stem cells. *Biomicrofluidics* **2019**, *13*, 064111. [CrossRef]
8. Guerin, N.; Lévesque, M.; Therriault, D. Helical dielectrophoretic particle separator fabricated by conformal spindle printing. *J. Biomed. Sci. Eng.* **2014**, *7*, 641–650. [CrossRef]
9. Martinez-Duarte, R. Microfabrication technologies in dielectrophoresis applications—A review. *Electrophoresis* **2012**, *33*, 3110–3132. [CrossRef]
10. Natu, R.; Martinez-Duarte, R. Numerical model of streaming DEP for stem cell sorting. *Micromachines* **2016**, *7*, 217. [CrossRef]
11. Urdaneta, M.; Smela, E. Multiple frequency dielectrophoresis. *Electrophoresis* **2007**, *28*, 3145–3155. [CrossRef] [PubMed]
12. Park, S.; Koklu, M.; Beskok, A. Particle trapping in high-conductivity media with electrothermally enhanced negative dielectrophoresis. *Anal. Chem.* **2009**, *81*, 2303–2310. [CrossRef] [PubMed]
13. Nedelcu, O.T. A Thermal study on Joule-heating induced effects in dielectrophoretic microfilters. *Rom. J. Inf. Sci. Technol.* **2011**, *14*, 309–323.
14. Lu, Y.; Ren, Q.L.; Liu, T.T.; Leung, S.L.; Gau, V.; Liao, J.C.; Chan, C.L.; Wong, P.K. Long-range electrothermal fluid motion in microfluidic systems. *Int. J. Heat Mass Transf.* **2016**, *98*, 341–349. [CrossRef]
15. Pethig, R. Dielectrophoresis: Status of the theory, technology, and applications. *Biomicrofluidics* **2010**, *4*, 022811. [CrossRef]
16. Al-Ahdal, S.A.; Kayani, A.B.; Ali, M.A.M.; Chan, J.Y.; Ali, T.; Adnan, N.; Buyong, M.R.; Noor, E.E.M.; Majlis, B.Y.; Sriram, S. Dielectrophoresis of amyloid-beta proteins as a microfluidic template for Alzheimer's research. *Int. J. Mol. Sci.* **2019**, *20*, 3595. [CrossRef]
17. Seger, U.; Panayiotou, M.; Schnydrig, S.; Jordan, M.; Renaud, P. Temperature measurements in microfluidic systems: Heat dissipation of negative dielectrophoresis barriers. *Electrophoresis* **2005**, *26*, 2239–2246. [CrossRef]
18. Lindquist, S. The heat-shock response. *Annu. Rev. Biochem.* **1986**, *55*, 1151–1191. [CrossRef]
19. Moritz, A.R. Studies of thermal injury: III. The pathology and pathogenesis of cutaneous burns: An experimental study. *Am. J. Pathol.* **1947**, *23*, 915–941.
20. Harmon, B.V.; Corder, A.M.; Collins, R.J.; Gobe, G.C.; Allen, J.; Allan, D.J.; Kerr, J.F.R. Cell-death induced in a murine mastocytoma by 42–47 degrees heating in vitro: Evidence that the form of death changes from apoptosis to necrosis above a critical heat load. *Int. J. Radiat. Biol.* **1990**, *58*, 845–858. [CrossRef]
21. Yamada, K.; Ichikawa, Y.; Okumura, H. Effects of high temperatures on chromosomes of normal and transformed human cells. *Hum. Cell* **1989**, *21*, 80–85.
22. Tay, F.E.H.; Yu, L.M.; Pang, A.J.; Iliescu, C. Electrical and thermal characterization of a dielectrophoretic chip with 3D electrodes for cells manipulation. *Electrochim. Acta* **2007**, *52*, 2862–2868. [CrossRef]
23. Sridharan, S.; Zhu, J.J.; Hu, G.Q.; Xuan, X.C. Joule heating effects on electroosmotic flow in insulator-based dielectrophoresis. *Electrophoresis* **2011**, *32*, 2274–2281. [CrossRef]
24. Nakano, A.; Luo, J.H.; Ros, A. Temporal and spatial temperature measurement in insulator-based dielectrophoretic devices. *Anal. Chem.* **2014**, *86*, 6516–6524. [CrossRef]
25. Williams, S.J.; Chamarthy, P.; Wereley, S.T. Laser-induced Fluorescence Thermometry for Joule Heating in AC Electrokinetic Chips. In Proceedings of the ASME 2008 Fluids Engineering Division Summer Meeting Collocated with the Heat Transfer, Energy Sustainability, and 3rd Energy Nanotechnology Conferences 2008, Jacksonville, FL, USA, 10–14 August 2008.
26. Chamarthy, P.; Garimella, S.V.; Wereley, S.T. Non-intrusive temperature measurement using microscale visualization tech-niques. *Exp. Fluids* **2009**, *47*, 159–170. [CrossRef]
27. Chamarthy, P.; Garimella, S.V.; Wereley, S.T. Measurement of the temperature non-uniformity in a microchannel heat sink using microscale laser-induced fluorescence. *Int. J. Heat Mass Transf.* **2010**, *53*, 3275–3283. [CrossRef]
28. Erickson, D.; Sinton, D.; Li, D.Q. Joule heating and heat transfer in poly (dimethylsiloxane) microfluidic systems. *Lab. Chip* **2003**, *3*, 141–149. [CrossRef]
29. Williams, S.J.; Chamarthy, P.; Wereley, S.T. Comparison of experiments and simulation of joule heating in ac electrokinetic chips. *Trans. ASME J. Fluids Eng.* **2010**, *132*, 021103. [CrossRef]
30. Tang, G.Y.; Yang, C. Numerical modeling of Joule heating-induced temperature gradient focusing in microfluidic channels. *Electrophoresis* **2008**, *29*, 1006–1012. [CrossRef]
31. Rasmussen, A.; Mavriplis, C.; Zaghloul, M.E.; Mikulchenko, O.; Mayaram, K. Simulation and optimization of a microfluidic flow sensor. *Sens. Actuators A* **2001**, *88*, 121–132. [CrossRef]

32. Gallo-Villanueva, R.C.; Perez-Gonzalez, V.H.; Cardenas-Benitez, B.; Jind, B.; Martinez-Chapa, S.O.; Lapizco-Encinas, B.H. Joule heating effects in optimized insulator-based dielectrophoretic devices: An interplay between post geometry and temper-ature rise. *Electrophoresis* **2019**, *40*, 1408–1416. [CrossRef] [PubMed]
33. Kwak, T.J.; Hossen, I.; Bashir, R.; Chang, W.J.; Lee, C.H. Localized dielectric loss heating in dielectrophoresis devices. *Sci. Rep.* **2019**, *9*, 18977. [CrossRef] [PubMed]
34. Wang, Q.R.; Dingari, N.N.; Buie, C.R. Nonlinear electrokinetic effects in insulator-based dielectrophoretic systems. *Electro-phoresis* **2017**, *38*, 2576–2586. [CrossRef] [PubMed]
35. Khoshmanesh, K.; Akagi, J.; Nahavandi, S.; Skommer, J.; Baratchi, S.; Cooper, J.M.; Kalantar-Zadeh, K.; Williams, D.E.; Wlodkowic, D. Dynamic analysis of drug-induced cytotoxicity using chip-based dielectrophoretic cell immobilization technology. *Anal. Chem.* **2011**, *83*, 2133–2144. [CrossRef]
36. Nagasaka, A.; Seki, Y.; Tomiyama, N.; Mori, U.; Eguchi, M.; Tada, S. Development of High-throughput Cell Separation Micro-fluidic Device Using Dielectrophoresis. In Proceedings of the 9th World Congress of Biomechanics 2022 Taipei, Taipei, Taiwan, 10–14 July 2022.
37. Wu, J.; Lian, M.; Yang, K. Micropumping of biofluids by alternating current electrothermal effects. *Appl. Phys. Lett.* **2007**, *90*, 3. [CrossRef]
38. Ren, Y.K.; Liu, W.Y.; Tao, Y.; Hui, M.; Wu, Q.S. On AC-field-induced nonlinear electroosmosis next to the sharp cor-ner-field-singularity of leaky dielectric blocks and its application in on-chip micro-mixing. *Micromachines* **2018**, *9*, 102. [CrossRef]
39. Akutsu, D.; Motosuke, M.; Honami, S. A Study on Particle Manipulation in Microchannel with High Frequency AC Electrokinetics. In Proceedings of the Japan Society of Mechanical Engineers; the Fluids Engineering Conference 2009, Nagoya, Japan, 7–8 November 2009.
40. McAdams, W.H. *Heat Transmission*, 3rd ed.; McGraw-Hill Book Company: New York, NY, USA, 1954.
41. Fishenden, M.; Saunders, O.A. *An Introduction to Heat Transfer*; Oxford University Press: Oxford, UK, 1950.
42. Alarabi, M.; Elriedy, M.K. Natural-convection heat-transfer from isothermal horizontal plates of different shapes. *Int. J. Heat Mass Transf.* **1976**, *19*, 1399–1404. [CrossRef]
43. Yousef, W.W.; Tarasuk, J.D.; Mckeen, W.J. Free convection heat transfer from upward-facing isothermal horizontal surfaces. *Trans. ASME J. Heat Transf.* **1982**, *104*, 493–500. [CrossRef]
44. Shah, R.K.; London, A.L. *Laminar Flow Forced Convection in Ducts, Advances in Heat Transfer, Supplement 1*; Academic Press: New York, NY, USA, 1978.
45. Elengoe, A.; Alitheen, N.B.M.; Hamdan, S.B. Hyperthermia effect on human normal breast (MCF-10A) and cancer (MDA-MB 231 and MCF-7) cells. *Asian J. Pharm. Clin. Res.* **2019**, *12*, 512–515. [CrossRef]
46. Pulavarthy, R.A.; Alam, M.T.; Haque, M.A. Effect of heated zone size on micro and nanoscale convective heat transfer. *Int. Commun. Heat Mass Transf.* **2014**, *52*, 56–60. [CrossRef]
47. Knupp, D.C.; Naveira-Cotta, C.P.; Renfer, A.; Tiwari, M.K.; Cotta, R.M.; Poulikakos, D. Analysis of conjugated heat transfer in micro-heat exchangers via integral transforms and non-intrusive optical techniques. *Int. J. Numer. Methods Heat Fluid Flow* **2015**, *25*, 1444–1462. [CrossRef]

Disclaimer/Publisher's Note: The statements, opinions and data contained in all publications are solely those of the individual author(s) and contributor(s) and not of MDPI and/or the editor(s). MDPI and/or the editor(s) disclaim responsibility for any injury to people or property resulting from any ideas, methods, instructions or products referred to in the content.